# Stability and heat transfer characteristics of unsteady condensing and evaporating films

Sanjoy M. Som [a,*], Jeramy T. Kimball [a], James C. Hermanson [a], Jeffrey S. Allen [b]

[a] *Department of Aeronautics and Astronautics, University of Washington, Seattle, WA 98195, United States*
[b] *Department of Mechanical Engineering, Michigan Technological University, Houghton, MI 49931, United States*

## Abstract

The stability and heat transfer characteristics of an unsteady condensing and evaporating $n$-pentane film on the underside of a cooled, flat, horizontal plate was studied experimentally. Unsteady conditions were produced by varying the system pressure in a cyclic fashion. The film was imaged using a double-pass shadowgraph system, and an embedded heat flux sensor measured the spatially averaged heat flux. Surface conditions were obtained using an inverse method. Images and data point collection were synchronized to permit direct correlation between thermal data and film behavior. The heat flux was affected by the Rayleigh–Taylor instability after an initial rise due to condensate formation. Hysteresis was observed in the heat flux over each pressure variation cycle, where the heat flux during condensation varied differently with the degree of subcooling than during evaporation. An additional study examined the film stability of non-condensing, growing films with mass addition but without thermal effects. Experiments showed that the film thickness at the point of first droplet break-off increased with increased pumping rate.
© 2006 Elsevier Ltd. All rights reserved.

*Keywords:* Unsteady film condensation; Rayleigh–Taylor instability; Microgravity; Mass addition; Condensation heat transfer; Film stability; Hysteresis

## 1. Introduction

Early studies of condensation include the examination of steam condensing on a vertical surface by Nusselt in 1916 [1]. Numerous studies of film condensation and evaporation have since been performed under a variety of conditions and geometries [2–7]. Another problem of fundamental interest is film condensation on the underside of a flat plate. A downward-facing film is inherently unstable due to the Rayleigh–Taylor instability [8]. This instability results in the formation of waves on the liquid film, as sketched in Fig. 1. These waves continue to grow until pendant drops form. Surface tension tends to retard the process. The process can be further retarded by the increased condensation at the troughs of the waves due to the local thinning and the corresponding higher condensation rate of the saturated vapor onto the instability induced wavy film. However, the impact of any non-uniform condensation on the stability of the film is generally negligible in normal gravity compared to the body force [9,10].

Condensation on the underside of a plate has been studied extensively [11–14]. Although studies of unsteady processes of film condensation do exist in the literature [15], a majority of previous investigations have generally been performed at conditions of constant vapor pressure and temperature, and thus studied the stability and heat transfer of *steady state* systems. The study of film condensation and evaporation in the presence of a cyclically varying pressure is important to understand the startup and shutdown process of engineering devices that rely on phase change. Batch processing systems in a low-gravity environment could be particularly vulnerable to transient instabilities [16].

---

* Corresponding author. Present address: Department of Earth and Space Sciences, University of Washington, Seattle, WA 98195, United States. Tel.: +1 206 685 1707; fax: +1 206 543 0489.
*E-mail address:* sanjoy@u.washington.edu (S.M. Som).

Nomenclature

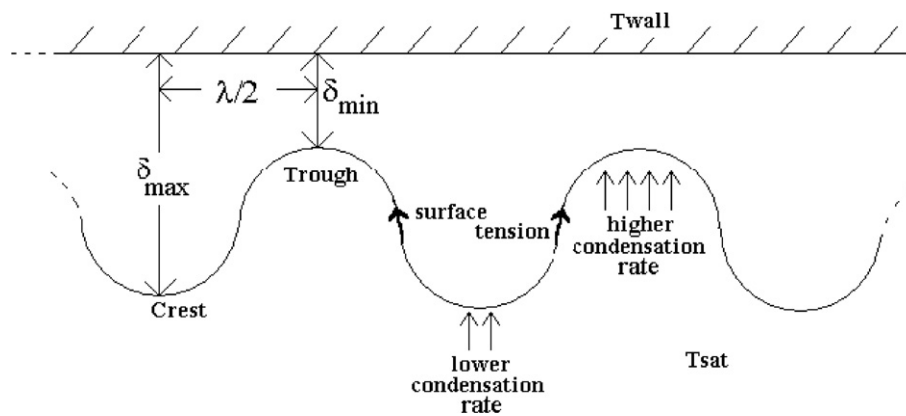| | | | |
|---|---|---|---|
| $A$ | exposed plate area | $\mu$ | dynamic viscosity of the liquid |
| $g$ | acceleration due to gravity | $v$ | kinematic viscosity of the liquid |
| $\bar{h}$ | average heat transfer coefficient | $\theta$ | inclination angle of the condensing surface liquid |
| $h_{fg}$ | enthalpy of vaporization | | |
| $k$ | coefficient of thermal conductivity | $\rho$ | density |
| $L_{c\theta}$ | capillary length | $\sigma$ | surface tension |
| $\Delta T$ | degree of film subcooling, $T_{sat} - T_{wall}$ | $\sigma_T$ | temperature derivative of the surface tension |
| $t$ | time | $\tau$ | characteristic time of pendant drop break-off |
| $T$ | temperature | | |
| $\dot{V}$ | volume flow rate | *Subscripts* | |
| $v$ | flow velocity | h | hole (for perforated plate) |
| | | l | liquid |
| *Greek symbols* | | v | vapor |
| $\delta$ | layer (film) thickness | sat | saturated |
| $\bar{\delta}$ | mean film thickness | wall | wall |
| $\lambda$ | instability wavelength | | |



Fig. 1. Illustration of instability-waves.

Applications of condensation and evaporation include two-phase thermal control systems found in space and terrestrial applications for environment control and life support (e.g. humidity control, air revitalization, water purification, and heat rejection), as well as thermal management of spacecraft components (e.g. heat pipes) [16–19]. The behavior of films undergoing condensation and/or evaporation needs to be explored further, especially in light of the recent focus on human exploration of the Moon and Mars. Indeed, applications of this science are crucial for long-term space exploration, which depend heavily on two-phase fluid mechanics and heat transfer [16,17].

The overall objective of the current research is the examination of film condensation and evaporation under reduced-gravity conditions. Microgravity is beneficial from a fluid mechanics standpoint in that it permits examination of thermocapillary phenomena and vapor recoil by significantly reducing the body forces that drive buoyancy. Reduced-gravity also slows down the instability process thus yielding increased insight on the process since the crit-

ical wavelength of the most unstable disturbance increases with decreasing gravity level in inverse proportion to $g^{1/2}$ [20]. The reduced gravity duration (20–30 s) afforded by parabolic aircraft flights requires understanding of unsteady conditions in the laboratory environment, serving as an additional motivation for the unsteady laboratory experiments presented in this paper.

## 2. Experimental configurations

Two experimental configurations were employed in this study: an enclosed test cell in which condensation and evaporation occurred on the underside of a flat plate, and a perforated surface through which a nonvolatile fluid was pumped to simulate a condensing film. In the former case, unsteady film condensation and evaporation were produced by the cyclic variation of the system pressure. The behavior of the film was examined both visually and by measurement of temperatures as well as heat flux. In the latter experimental configuration, film growth due to condensation was

simulated by pumping silicone oil through a perforated plate, enabling the study of pendant drop size, instability wavelengths, and time of initial pendant drop break-off in the absence of thermal and phase change effects. The impact of the fluid flow through the perforations on the bulk film can be characterized in terms of the Weber number,

$$We = \frac{\rho v_h^2 d_h}{\sigma}. \tag{1}$$

The Weber numbers for the pumped-film conditions of these experiments ranged from $We = 7 \times 10^{-4}$ to $We = 3 \times 10^{-2}$. These values of Weber number are substantially below the value of $We = 1$, above which disturbances to the film can be expected [21]. Additional insights on condensing film physics were gained by making the correlation between the pumping rate of the silicone oil and the actual condensation rate of $n$-pentane.

## 2.1. Condensation/Evaporation experimental setup

The setup for condensation/evaporation experiments is illustrated in Figs. 2 and 3. The test chamber was a 60 in.$^3$ (683 cm$^3$) aluminum circular cylindrical shell 3 in. (7.6 cm) tall. A circular 1/2 in. (1.27 cm) thick transparent Pyrex glass plate comprised the bottom of the test cell to permit optical access to the condensing surface. The condensing surface was a 0.15 in. (3.81 mm) thick, 4 in. (10.16 cm) in

diameter polished brass cover plate bonded using high conductivity epoxy ($k = 1.59\ \mathrm{W m^{-1}\ K^{-1}}$) onto a 1.5 in. (3.81 cm) thick brass block with a heat flux sensor sandwiched between the two. The entire test cell was hermetically sealed from outside air. Brass was chosen over copper as the condensing surface material because of its lower thermal conductivity, which permits the measurement of $\Delta T$ even across relatively thin sections. An additional advantage is that brass does not scratch as easily as copper.

Evaporating $n$-pentane ($C_5H_{12}$) in a 500 ml degassed Pyrex container provided the vapor for the experiment. $N$-pentane was selected as the working fluid due to its excellent wettability characteristics, its high vapor pressure, and its low boiling point (36 °C). The temperature of the liquid $n$-pentane in the vapor generator was held at a fixed value by a temperature controller connected to a thermocouple immersed in the fluid.

An embedded thin-film heat flux sensor was used to measure heat flux and temperature to preclude disturbances to the condensing films. The heat flux sensor was separated from the exposed surface by a brass cover plate 0.16 in. (4 mm) thick. The dimensions of the sensor were 1.38 in × 1.06 in. (3.5 cm × 2.7 cm) which exceed the instability wavelength by a factor of two in both dimensions as discussed below. The sensor was ringed by a Kapton layer of identical thickness and thermal conductivity to ensure uniform thermal resistance across the cross section of the brass block. The entire cover plate/heat flux sensor/block assembly was cured under vacuum to remove air bubbles trapped in the epoxy between the block and plate, the sensor and the block, and the sensor and the plate, to minimize the thermal resistance between the different elements. No solid–solid interfaces thus exist, minimizing the contact resistance between the different elements. The minor contribution to the overall thermal resistance from the adhesive layers was estimated to result in a change in the surface temperature of roughly 0.3 °C, which is comparable to the accuracy of the thermocouples. Additional thermal measurements included a thermocouple imbedded near the surface and two thermocouples within the chamber to measure vapor temperature. The cover plate was polished to improve imaging quality. The cooled plate assembly is shown in Fig. 4. A 1/2 in. (1.27 cm) deep serpentine
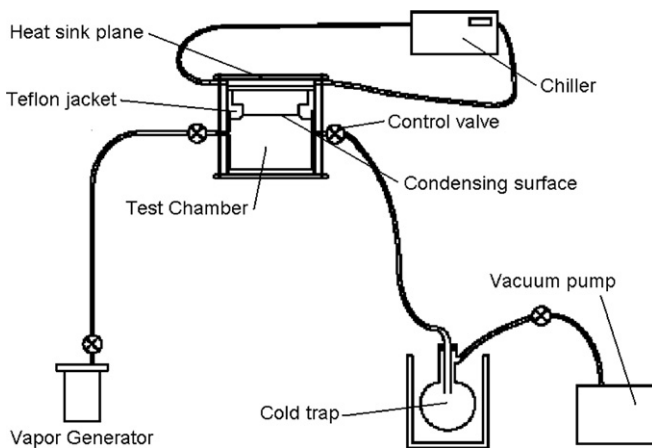


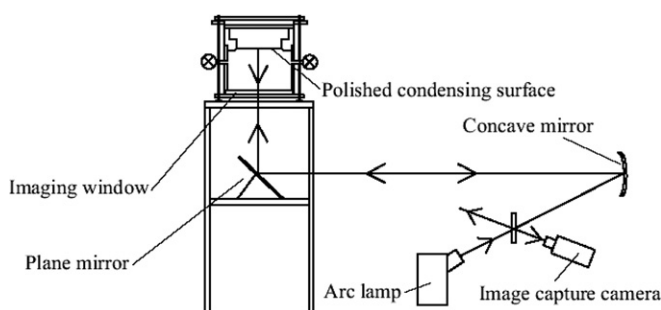Fig. 2. Experimental setup: hydraulics.
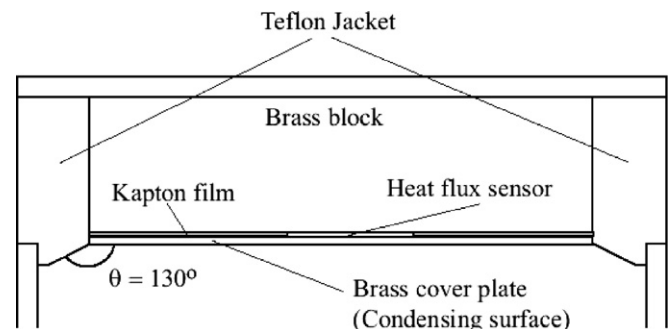


Fig. 3. Experimental setup: optics.



Fig. 4. Detail illustration of the condensing surface.

channel was milled on top of the cooling block to allow the flow of temperature-controlled water from a circulating refrigeration unit to maintain a constant temperature plane. The channel surface is referred to as the *heat sink plane* (Fig. 2). Through heat conduction, the brass achieved uniform surface temperature to within ±0.1 °C as verified using a surface temperature probe.

To minimize heat transfer with the environment, a 1 in. (2.54 cm) thick Teflon jacket insulated the cooled brass block. The Teflon jacket was chamfered at an angle of 130° to keep the film surface nearly parallel to the condensing surface at the boundaries, as shown in Fig. 4. The diameter of the condensing surface was chosen to be sufficiently large to minimize edge effects. Yanadori [12] found that to accomplish this, the condensing surface dimension must be less than twice the minimum wavelength $\lambda$ given by[1]

$$\lambda = 2\pi\sqrt{\frac{\sigma}{g(\rho_l - \rho_v)}} \qquad (2a)$$

for boundary conditions to affect the heat transfer. Eq. (2a) gives a 9.4 mm wavelength for *n*-pentane, which is significantly less than the diameter of the condensing surface (10.2 cm). A more precise expression has been developed [10] for the characteristic wavelength of liquid films sufficiently thick to avoid rupture:

$$\lambda = 2\pi\sqrt{2}\sqrt{\frac{\sigma}{g(\rho_l - \rho_v)}} \qquad (2b)$$

which for *n*-pentane gives a wavelength of 13.2 mm; again, significantly less than the diameter of the exposed, cooled surface employed in this work. In addition, the spatially averaged heat flux was measured at the center of the cooled surface, which is insensitive to boundary effects.

The cyclic variation of the system pressure was accomplished using an electronic pressure regulator (EPR). The EPR has computer-based user inputs (maximum pressure, minimum pressure and period for the cyclic case) and matches the pressure in the cell using feedback from a pressure transducer located in the test chamber. The measured pressure was within 5% of the desired value at any given point in the cycle.

Before vapor was introduced, a vacuum pump was used to evacuate air from the test cell. High vapor purity was achieved and maintained by minimizing air leaks and allowing a constant flow of pure vapor through the system. The pump was kept running throughout the experiment. To minimize the amount of vapor entering the pump, the test vapor exiting the test cell was frozen and contained in a liquid nitrogen cold trap. The entire experimental setup was enclosed in a sheet metal enclosure ventilated by explosion-proof fans and was monitored for leaks by combustible gas detectors.

---

[1] The original equation given in that work contained a typographical error which has been corrected here.

## 2.2. Optical system

The condensing surface was imaged using a double-pass shadowgraph system (Fig. 3). Light from an arc lamp passed through a beam splitter onto a concave mirror, which formed a parallel beam. A flat mirror deflected the beam onto the condensing surface. The light reflecting off the surface followed the same path back to the beam splitter where a 45 mm lens attached to a Panasonic Super-Dynamic II video camera capable of 771 × 492 pixels captured the reflected image. The spatial resolution was approximately 0.2 mm per pixel. The camera was connected to a computer containing image capture and recording capabilities. The double-pass shadowgraph method readily revealed perturbations at the liquid/vapor interface but also exaggerated any imperfections on the exposed surface.

## 2.3. Data acquisition

To minimize sensor noise, each channel was sampled at 10 kHz and 2000 samples were averaged for each recorded datum. The thermocouples, pressure transducer and heat flux sensor were all connected to a signal conditioning interface, which was connected to a data acquisition (DAQ) card in a computer. The DAQ software also coordinated the image acquisition. The data acquisition system was designed such that each thermal data point had an accompanying image of the condensing film to allow correlation between the film behavior and heat transfer characteristics.

## 2.4. Numerical correction for the surface heat flux

The heat flux sensor was not located on the condensing surface but was embedded 0.15 in. (3.81 mm) beneath the surface to avoid disturbing the homogeneous condensing surface. In order to determine the actual heat flux at the surface, we used a numerical inverse method [22–24]. Such methods are often employed when direct measurements of surface conditions are not possible [24]. In this method the physical domain was divided into two regions. The first, or *direct*, region is between the heat sink plane and the heat flux sensor. This problem is well defined. The second, or *inverse*, region is between the heat flux sensor and the condensing surface. In this region, a central-differencing method was employed to discretize the domain and a linear least-squares method was adopted to estimate the surface heat flux. The time domain was discretized using a backward differencing scheme. From experimentally acquired data, an average cycle was computed. The representative average cycle was fitted with a smoothing spline to obtain an acceptable analytical fit. The smoothing spline algorithm minimizes (1) the sum of the square of the residuals and (2) the integral of the curvature of the fit with parametric weighting for each. This fit then served as the code input

along with similar spline fitting of the measured temperature of the heat flux sensor.

### 2.5. Pumped-film experimental setup

The experimental test cell for the pumped-film experiments was composed of a hollow brass circular cylinder containing a stack of six 3.94 in. (10 cm) in diameter microperforated steel plates with 361 0.0098 in. (0.25 mm) diameter holes 0.125 in. (3.175 mm) apart. The pores were designed to keep the Weber number low to minimize disturbances to the growing surface during pumping, as discussed previously.

Silicone oils with different viscosities (50cSt and 125cSt) were pumped at different rates (2 ml/min, 4 ml/min, 8 ml/min, and 12 ml/min) into the cell using a syringe pump. The 12 ml/min rate gave a film thickness growth rate comparable to that expected for the condensing films; the other pumped films grew more slowly than the condensing film. The behavior of the non-condensing, growing films provides some insight into the mechanisms operative on condensing films, as discussed below. The pumped-film experimental data consisted of images obtained using the double-pass shadowgraph system.

## 3. Condensation experiment – results

### 3.1. Steady condensation

The experiment was first run at a series of constant pressures, varying from 60 kPa to 75 kPa in steps of 5 kPa. The measured quasi-steady state heat transfer is shown compared to those of Gerstmann [11] (who used R-113 and water) in Fig. 5. The Nusselt and Rayleigh numbers are defined here as

$$Nu \equiv \frac{\bar{h}}{k_l} L_{c\theta}^2 \tag{3}$$

$$Ra \equiv \frac{\sigma \rho_l h_{fg}}{k \mu_l \Delta T} L_{c\theta} \tag{4a}$$

where the capillary length is defined as

$$L_{c\theta} \equiv \sqrt{\frac{\sigma}{g(\rho_l - \rho_v)\cos(\theta)}} \tag{4b}$$

The solid lines A and B in Fig. 5 refer to Eqs. (5) and (6), respectively [11]

$$\overline{Nu} = 0.81 Ra^{0.193}; \quad 10^{10} > Ra > 10^9 \tag{5}$$

$$\overline{Nu} = 0.69 Ra^{0.20}; \quad 10^8 > Ra > 10^6$$

$$\overline{Nu} = \frac{0.90 Ra^{1/6}}{1 + 1.1 Ra^{-1/6}}; \quad 10^6 > Ra \tag{6}$$

The variation of the liquid dynamic viscosity, liquid density, saturated vapor density, and surface tension with temperature for n-pentane are available in the literature [25–27]. The heat transfer results plotted in Fig. 5 show the current results agree well with the correlations suggested by Gerstmann and Griffith [11], thus validating our experimental apparatus.

### 3.2. Cyclic condensation and evaporation

#### 3.2.1. Experimental results

The experiments were run with pressures varying sinusoidally between $P_{min} = 38$ kPa ($T_{sat} = 283$ K) and $P_{max} = 50$ kPa ($T_{sat} = 289.5$ K) with a 180 s cycle period. These test parameters were selected to ensure that each cycle reached both the continuous film condition and a fully dry surface. To achieve a dry surface, the temperature of the exposed surface during minimum pressure was set above the corresponding saturation temperature. The cycle time of 180 s was the minimum time that allowed the actual system pressure to closely follow the specified sinusoidal path.

Three sets consisting of 8–10 cycles each were performed with the heat sink plane (the cooled end of the brass block assembly) temperatures varying from 10 °C to 14 °C in increments of 2 °C. For a heat sink plane temperature of 15 °C, the saturation temperature corresponding to $P_{max}$
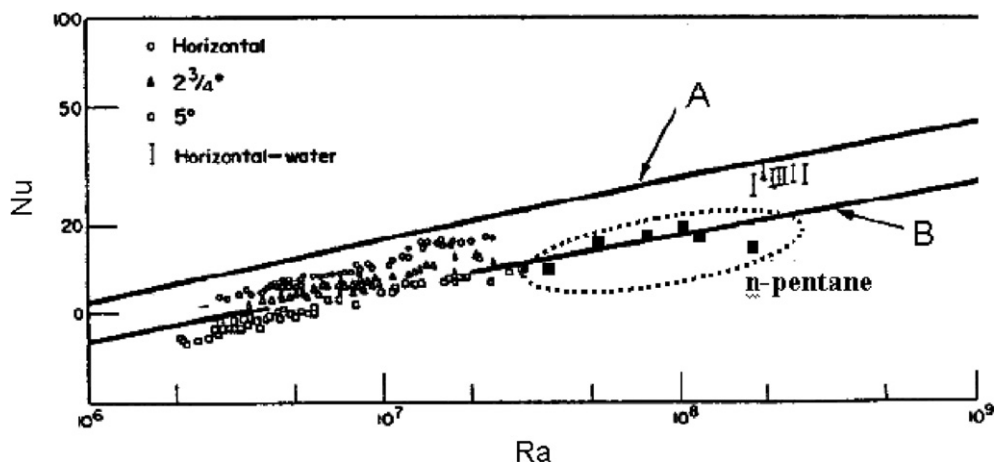


Fig. 5. Comparison of n-pentane steady-state heat transfer with Gerstmann [11]. The results are within the dashed region shown.

was slightly cooler than the condensing surface temperature, and no film was observed to form.

Fig. 6 shows that the cyclic variation in measured heat flux closely matches the period defined by the cyclically varying pressure, with a lag time of 1–9 s. The lag is attributed to the combined thermal mass of the cover plate and the thermal resistance of the sensor plane.

The surface heat flux and temperature determined by the inverse method over a typical cycle are shown along with the measured values in Fig. 7a–c. Also shown is the time
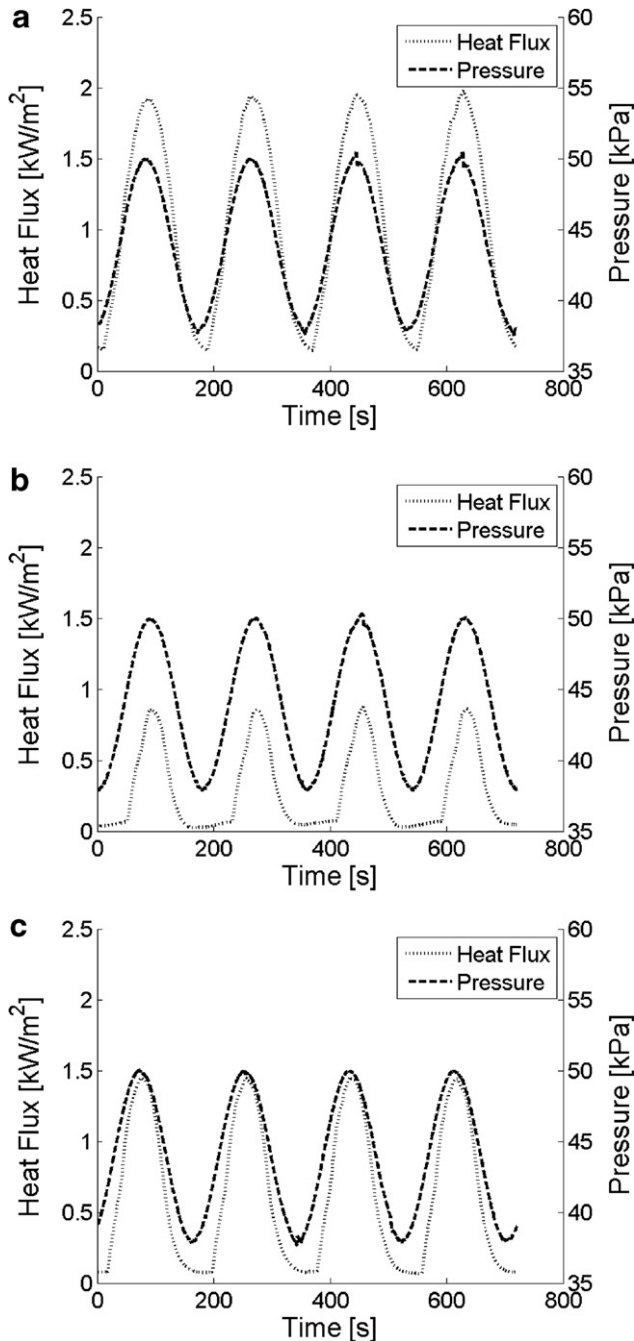


Fig. 6. Measured heat flux and pressure over several cycles (a) Heat sink plane temperature: 10 °C. (b) Heat sink plane temperature: 12 °C. (c) Heat sink plane temperature: 14 °C.

variation in the degree of subcooling. The highest value of the subcooling occurs at the point of pendant drop break-off (C), and is observed to be similar in all cases. The higher condensation rate on a colder wall in this unsteady process leads to increased heat flux and thus has a greater impact on the wall temperature, driving $T_{wall}$ to values similar to those obtained in the warmer plate experiments, where the lower condensation rate due to the warmer wall affects wall temperature to a lesser degree. During the evaporation that commences between points C and D, the decreasing pressure drives the saturated vapor temperature down in all cases. However, in the case of a warm exposed surface, the corresponding wall temperatures approach those of the heat sink plane near the end of the evaporation portion of the cycle, while the corresponding saturated vapor temperatures continue to drop. The subcooling thus becomes more negative for the case of warmer condensing surfaces, as seen in Fig. 7.

The surface heat flux is observed to increase as the pressure increases (and there is an increase in the corresponding saturation temperature) and decrease as the pressure decreases (corresponding to a decrease in the saturation temperature), and thus responding as generally expected to changes in ambient conditions. The maximum heat flux is observed to decrease as the heat sink plane temperature is increased, from a maximum value of 2.8 kW/m² to 1.6 kW/m² as the heat sink plane temperature increases from 10 °C to 14 °C. The waviness in the calculated surface heat flux seen in some cases is due to a combination of the fitting method and the sensitivity of the inverse code to the input conditions. Note that at location D in Fig. 7a–c, the heat flux is actually *negative*. This is due to the strong heat absorption by the film during evaporation as vapor temperature (driven by the decreasing presure) drops down below the wall temperature.

Image and data synchronization permitted correlation of the shadowgraph images with the measured and calculated temperature and heat flux. Examining the averaged cycles and matching them with the images taken (Fig. 8a–f) permitted identification of film behavior with the corresponding heat flux.

The film evolution and behavior were similar for all test cases. At time *A* (as indicated in Fig. 7), the saturation temperature rises above the surface temperature and the heat flux is seen to suddenly rise due to the condensate film forming on the surface. Shortly after the initial development of the film, a plateau in the surface heat flux is reached and the surface heat flux is seen to increase more slowly for large subcooling, stay constant, or begin to decrease slightly, corresponding to large subcooling (Fig. 7a), medium subcooling (Fig. 7b), and small subcooling (Fig. 7c), respectively. This relates to the increase in stable film thickness. At time B, the Rayleigh–Taylor instability becomes evident and culminates with pendant drop formation at point C.

The significant increase in the heat flux that corresponds to the apparent onset of Rayleigh–Taylor instability leading
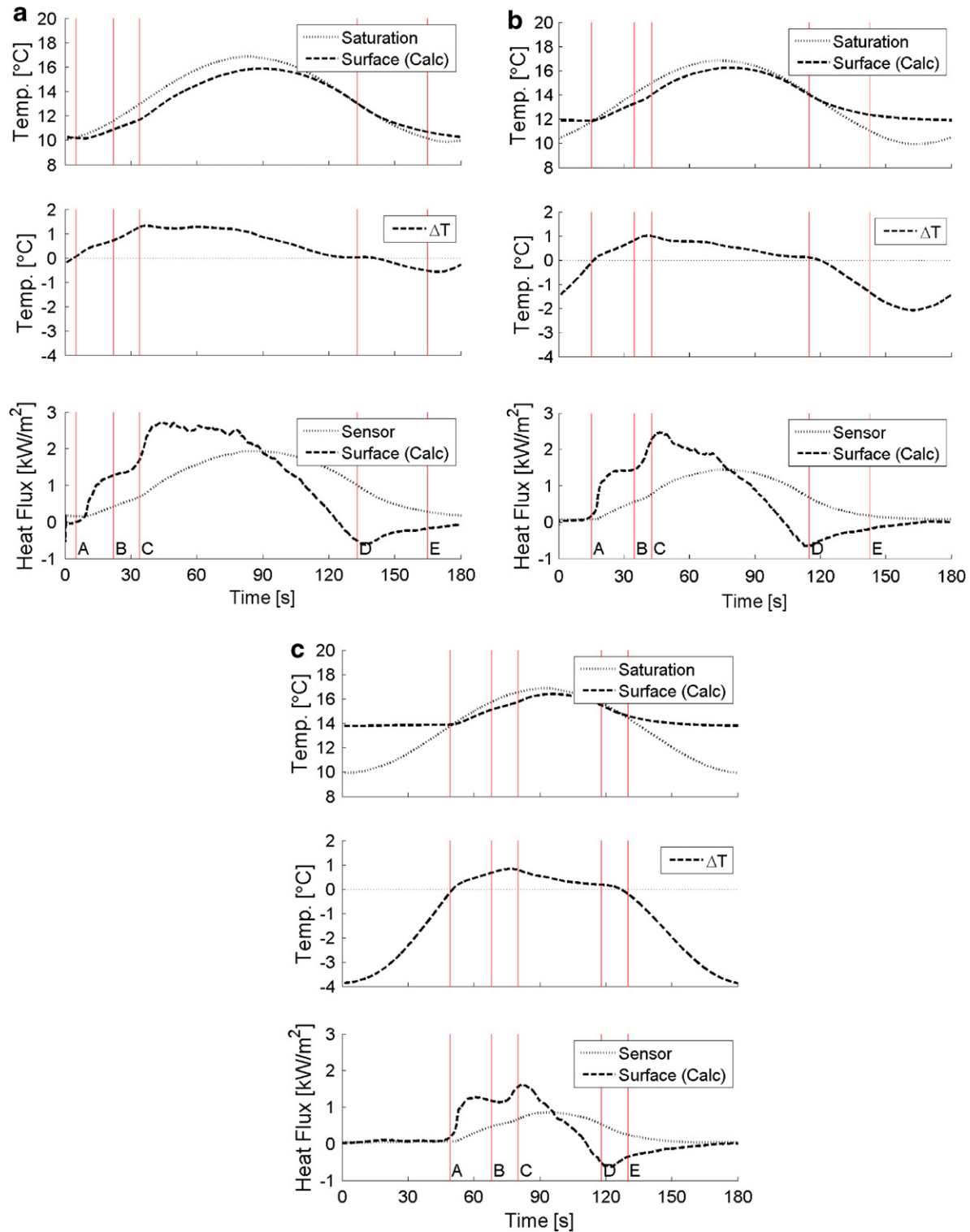
Fig. 7. Data-Image correlation of one cycle. Letters correspond to images in Fig. 8. (a) Heat sink plane temperature: 10 °C. (b) Heat sink plane temperature: 12 °C. (c) Heat sink plane temperature: 14 °C.

to pendant drop formation is consistent with the more rapid condensation that would be expected in the thinner regions of the troughs resulting from the Rayleigh–Taylor instability in the unstable film. As the drops break off, the film reaches a quasi-steady state and heat flux remains relatively

constant near point C, before the onset of evaporation as the system pressure decreases. This is evident in the 10 °C and 12 °C heat sink plane experiments (Fig. 7a and b) but was not fully achieved in the 14 °C case (Fig. 7c). The sequence of images taken show a higher rate of drop break-off with
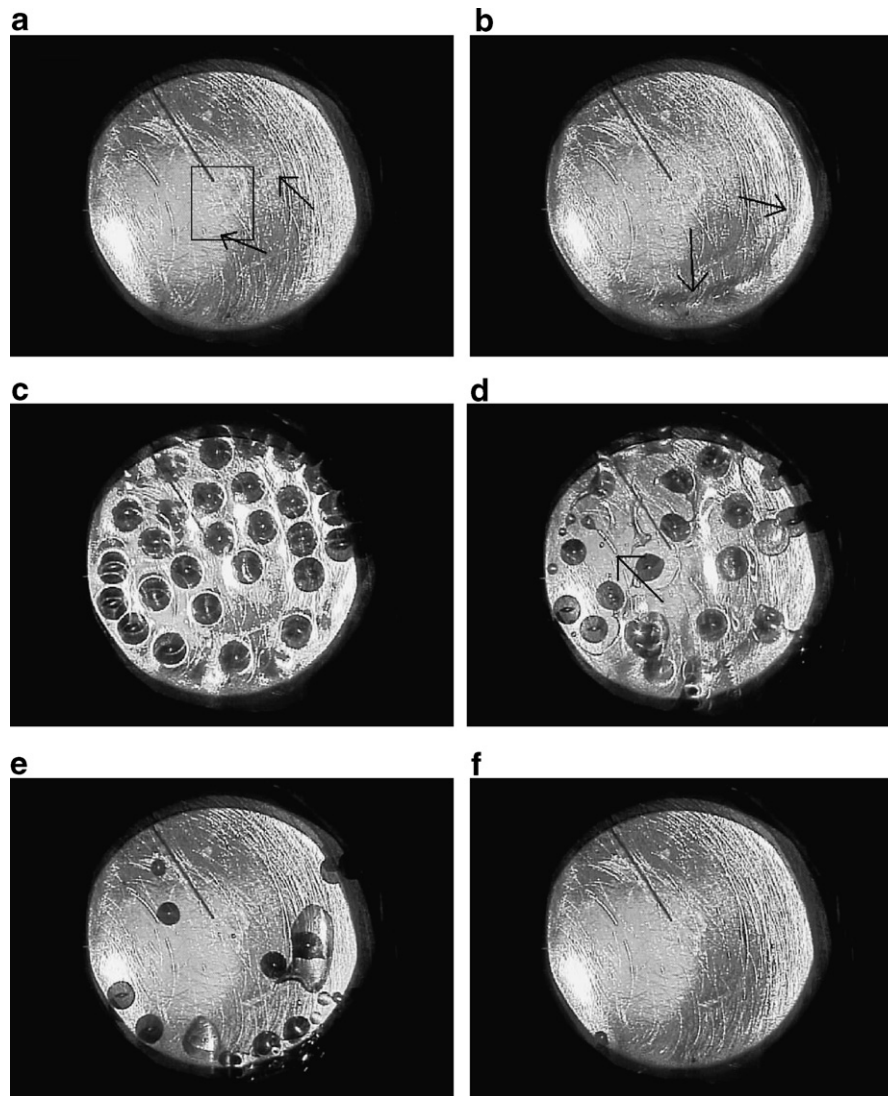
Fig. 8. Pictures corresponding to locations indicated in Fig. 7. (a) Shadowgraph picture taken at point A (arrows note film border and box shows approximate size of embedded probe). (b) Shadowgraph picture taken at point B (arrow shows instability occurring). (c) Shadowgraph picture taken at point C (complete drop coverage). (d) Shadowgraph picture taken at point D (arrow shows surface dry-out). (e) Shadowgraph picture taken at point E (surface is dry over sensor region). (f) Shadowgraph picture taken at point F (surface is fully dry).

higher subcooling, consistent with the higher heat flux and improving mass removal from the condensing surface. The surface heat flux is seen to rise significantly, in some cases doubling, after the onset of the Rayleigh–Taylor instability, peaking just after the pendant drops form, suggesting that film thickness, and the corresponding change in thermal resistance influences the heat flux variation to a greater extent than the actual degree of subcooling.

As the surface temperature approaches the saturation temperature the heat flux decreases, reaching a minimum when the surface temperature drops below the saturation temperature and the surface begins to dry out (D). The remnants of a few pendant drops still exist on the surface at point E and the heat flux approaches zero. Although the condensate film disappears quickly once the pressure drops, the pendant drops themselves require considerably more time to completely vaporize. The total time that the surface heat flux

is non-zero decreases with increasing heat sink plane temperature. This is evidently because higher wall temperature requires a higher saturation temperature and thus a higher system pressure; this is seen most clearly in Fig. 7a–c.

During the experiments with a higher degree of subcooling (Fig. 7a), the rise in heat flux is due to the film appearing on the surface. On the other hand, for lower subcooling (Fig. 7c), the heat flux initially increases slightly and gradually somewhat before the appearance of a fluid film. This is due to the natural convection inside the test cell where the vapor raises the temperature of the cooled surface (but not cool enough to cause condensation since the vapor temperature is still below that of the plate), which at the same time cools that vapor, which is replaced in turn by fresh, warmer vapor. For natural convection, the critical Rayleigh number is of the order $10^3$. In the current experimental configuration, a Rayleigh number in the order of $10^5$ was

computed with a temperature difference of 1 K between the saturated vapor temperature near the condensing surface (top) and the saturated vapor near the Pyrex glass (bottom). This suggests that convection is active within the test cell and could account for the gradual increase in heat transfer at low subcooling described earlier.

### 3.2.2. Hysteresis

Although studies examining reversibility and hysteresis in heat transfer have been conducted [28], they have not dealt with laminar film condensation and evaporation to our knowledge. The relationship between the heat flux and the degree of subcooling over an entire cycle is shown in Fig. 9. The data shown are based on the values of temperature and heat flux at the surface. The heat flux is generally not a unique function of the degree of subcooling but rather exhibits different behavior for the condensation and evaporation segments of each cycle. This effect is smallest in the 10 °C heat sink plane case. In the other cases, a pronounced "lobe" is seen in the area of highest subcooling (and highest heat flux). This lobe begins to form before the onset of instability (B), corresponding to the heat flux plateau described in Section 3.2.1 and is related to maximum stable film thickness. The heat flux rises again following local film thinning caused by the Rayleigh–Taylor instability and the formation of pendant drops. The loop is closed after the maximum heat flux is observed. Portions of the heat transfer curves from state A to B and from state C to D appear to follow similar paths. For this portion of the cycle, the film is thin compared with its thickness at the onset of Rayleigh–Taylor instability.

Significant hysteresis is also observed when the saturation temperature is below the exposed surface temperature, leading to negative values of heat flux. This hysteresis may be due in part to the fact that, while the bulk of the film evaporates before point D, there are still some pendant drops that are present as the pressure is dropping, while there are no drops initially present as the pressure is increasing. Changes in the flow convection in the vapor due to changes in the system pressure may also contribute to the observed hysteresis. The tail-like regions of nearly zero heat flux (most pronounced in Fig. 9c) are attributed to the portion of the cycle during which the vapor temperature is lower than the wall temperature, yielding minimal heat transfer in the absence of condensation. The hysteresis observed around the onset of the Rayleigh–Taylor instability seems to confirm that film thickness and interfacial behavior drives the heat flux more than the degree of subcooling, though both can directly affect the heat transfer at the surface.

### 3.3. Pumped film experiments

The development of non-condensing films created by pumping liquid through a perforated plate was also studied in this investigation. These tests started with a dry surface with silicone oil on the verge of exiting the micro-perforations, leading to film formation, film growth and the
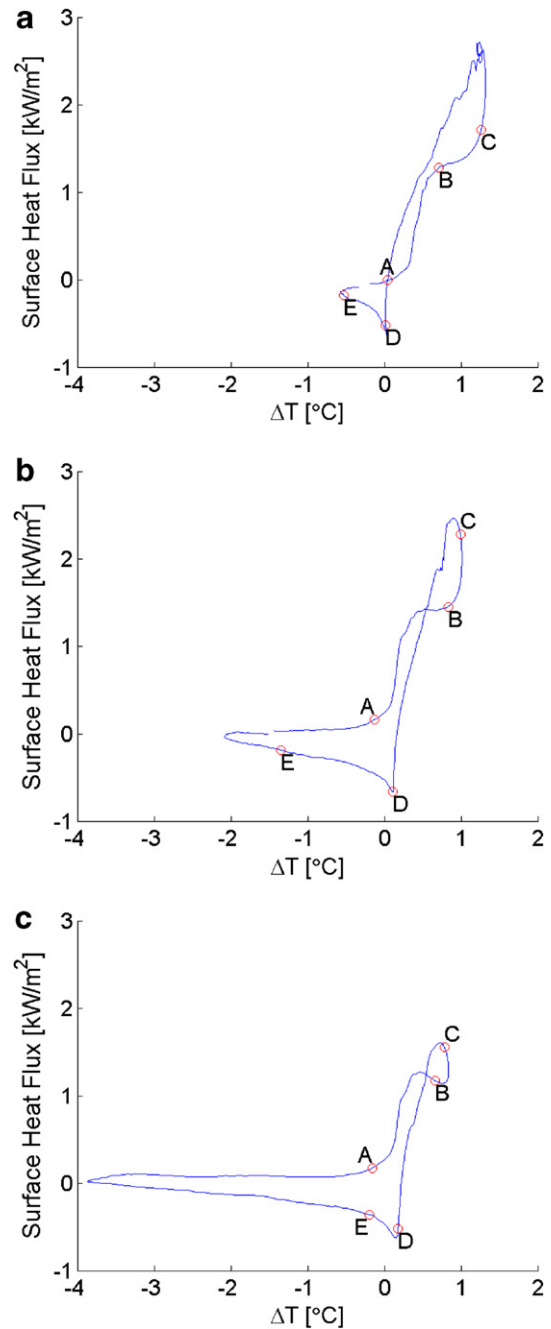


Fig. 9. Hysteresis in calculated surface heat flux versus calculated subcooling. (a) Heat sink plane temperature: 10 °C. (b) Heat sink plane temperature: 12 °C. (c) Heat sink plane temperature: 14 °C.

appearance and growth of instability waves, ending with the initial break-off of pendant drops. Imaging was employed to determine the drop formation and break-off time to an accuracy of 100 ms. The images were also used to determine formation wavelengths, pendant drop size and spacing, and drop evolution versus time for different pumping rates. The average film thickness at a given time can be computed by

$$\bar{\delta} = \frac{\dot{V} \times \tau}{A}. \tag{7}$$

The times to first pendant drop break-off are compared with those of condensing films in Table 1. The break-off times for the condensing and pumped films are on the same order of magnitude, and most closely agree for the slow pumping rate. The range of pumping rates proved useful to identify the key stages of instability, as the entire process was slowed down (except for the 12 ml/min study case).

Fig. 10 shows that the time to first droplet break-off decreases with increasing pumping rate, as expected, and the more viscous oil takes more time before break-off occurs. It is also seen that the film thickness at first droplet break-off increases with increasing pumping rate (Fig. 11). From the analogy that higher pumping rate is related to

Table 1
Drop break-off time for cyclic condensation and pumped films

| Heat sink plane temp. (°C) | Time to first drop break-off (s) | Standard deviation (s) |
| --- | --- | --- |
| 10 | 29.4 | 1.08 |
| 12 | 30.9 | 2.1 |
| 14 | 35.7 | 4.7 |
| | | |
| 50cSt pumping rate (ml/min) | Time to first drop break-off (s) | Standard deviation (s) |
| 2 | 28.9 | 1.11 |
| 4 | 17.4 | 0.6 |
| 8 | 10.7 | 0.3 |
| 12 | 7.97 | 0.1 |
| | | |
| 125cSt pumping rate (ml/min) | Time to first drop break-off (s) | Standard deviation (s) |
| 2 | 35.2 | 1.6 |
| 4 | 21.7 | 0.9 |
| 8 | 14.9 | 1.5 |
| 12 | 12.4 | 0.6 |
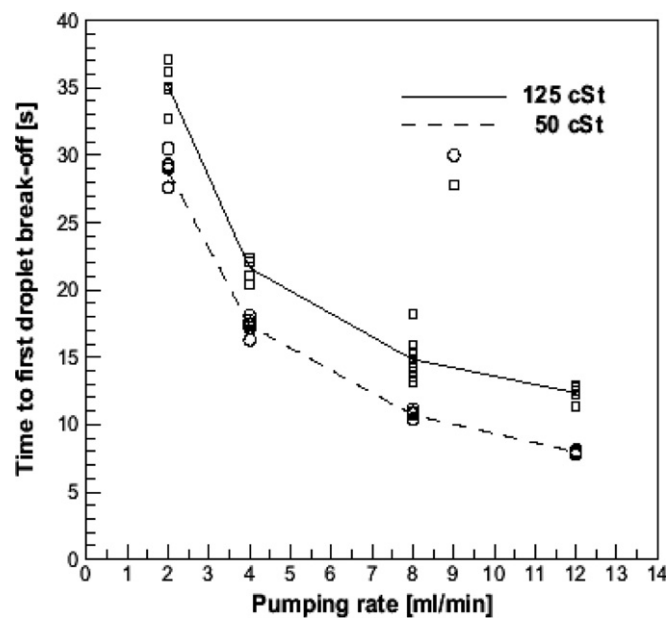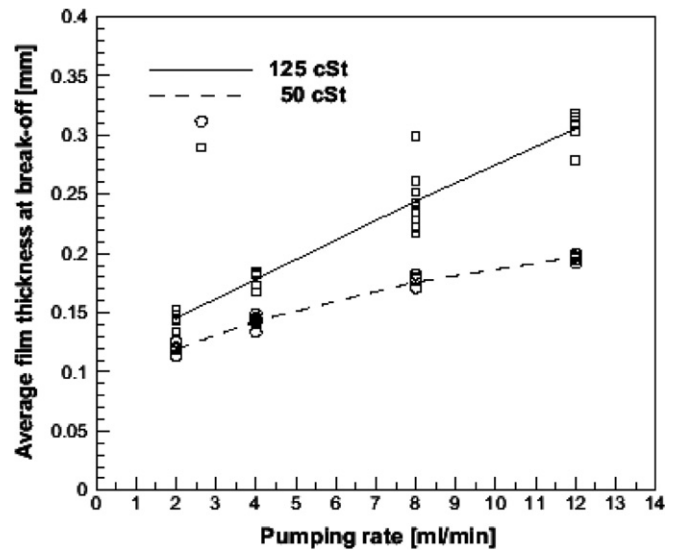


Fig. 11. Average film thickness at break-off vs. pumping rate for silicone oil at two different viscosities.

higher film growth rate, these results suggest that the higher condensation mass addition rate which occurs for higher degrees of subcooling may have a stabilizing effect on the pendant drop evolution.

Furthermore, these results suggest that, when subcooling is increased, the film thickness at first pendant drop break-off in the condensing film increases. However, no change in instability wavelength or drop size or spacing was observed between the different pumping rates or between the two silicone oils. Therefore, pumping rates (or subcooling differences) do not appear to influence drop size and instability wavelength.

### 4. Conclusion

This work experimentally studied the stability and heat transfer characteristics of a condensing and evaporating film on the underside of a cool, flat horizontal plate exposed to a vapor with a cyclically varying saturation pressure and temperature. An additional study was performed to examine film stability in the absence of thermal effects by pumping silicone oil through a perforated plate. The major conclusions are summarized as follows:

- Heat flux increases most dramatically due to the initial formation of a thin film of condensate. The spatially-averaged heat flux also appears to rise significantly at the appearance of the Rayleigh–Taylor instability and drop formation during a pressure ramp-up.
- In a cyclic pressure environment for a given range of saturation temperature, the variation in condensation surface temperature increases with decreasing heat sink plane temperature.
- Inverse methods can be successfully implemented to determine cyclic surface conditions with data from an embedded probe.



Fig. 10. Time to first break-off vs. pumping rate for silicone oil of two different viscosities.

- Hysteresis is exhibited in the case of cyclic pressure variation in the region of highest subcooling. The hysteresis loop closes after the onset of the Rayleigh–Taylor instability. The loop is likely due to the transient film thinning at the onset of the instability. Once the film is fully unstable, it reaches a quasi-steady state. The hysteresis suggests that film thickness has a greater influence than subcooling on the heat flux.
- Pumped-film experiments show that the film thickness at the point of first droplet break-off increases with increased pumping rate. No change in the instability wavelength with pumping rates was observed. Furthermore, since film thickness increases with higher pumping rate, it is suggested that rapid mass addition by condensation has a stabilizing effect on the Rayleigh–Taylor instability process.

## Acknowledgements

## References

[1] W. Nusselt, Die Oberflaechenkondensation des Wasserdampfes, Zeitschrift des Vereines Deutscher Ingenieure 60 (1916) 541–546, and 569–575.

[2] R.E. Johnson, A.T. Conlisk, Laminar-film condensation/evaporation on a vertically fluted surface, J. Fluid Mech. 184 (1987) 245–266.

[3] F. Blangetti, R. Krebs, Film condensation and evaporation in vertical tubes with superimposed vapor flow, Heat Exchange Sourcebook (1986) 449–465.

[4] S.M. Demsky, H.B. Ma, Thin film evaporation on a curved surface, Microscale Thermophys. Eng. 8 (3) (2004) 285–299.

[5] F.M. Joos, Thin liquid films on arbitrary surfaces with condensation or evaporation, in: ASME (Ed.), Proceedings of the Winter Annual Meeting of the American Society of Mechanical Engineers, New Orleans, LA, 1984, pp. 123–132.

[6] H.S. Wang, J.W. Rose, A theory of film condensation in horizontal noncircular section microchannels, J. Heat Transfer 187 (10) (2002) 1096–1105.

[7] H.C. Kang, M. H Kim, Characteristics of film condensation of supersaturated steam-air mixture on a flat plate, Int. J. Multiphase Flow 25 (8) (1999) 1601–1618.

[8] G.I. Taylor, The instability of liquid surfaces when accelerated in a direction perpendicular the their planes, Int. Proc. Roy. Soc. A 201 (1950) 192–196.

[9] J.P. Burelbach, S.G. Bankoff, S.H. Davis, Nonlinear stability of evaporating/condensing liquid films, J. Fluid Mech. 195 (1988) 463–494.

[10] S. Padate, J.S. Allen, J.C. Hermanson, Dynamics of evaporating films under reduced gravity, AIAA 44th Aerospace Science Meeting & Exhibit, Reno, NV, (AIAA-0738) (2006).

[11] J. Gerstmann, P. Griffith, Laminar film condensation on the underside of horizontal and inclined surfaces, Int. J. Heat Mass Transfer 10 (1967) 567–580.

[12] M. Yanadori, K. Hijikata, Y. Mori, M. Uchinda, Fundamental study of laminar film condensation heat transfer on a downward horizontal surface, Int. J. Heat Mass Transfer 28 (10) (1985) 1937–1944.

[13] S. Nozu, H. Inaba, H. Honda, T. Kobayashi, Experimental study of condensation heat transfer from a downward facing inclined surface, Heat Transfer Jpn. Res. 21 (1) (1992) 91–107.

[14] T. Li, S.G. Wang, P.T. Hsu, Laminar film condensation with constant heat flux on a finite-size horizontal plate, Chem. Eng. Commun. 172 (1999) 29–39.

[15] U. Schaflinger, Steady and unsteady process of film condensation of a flat plate, a vertical coin, a horizontal pipe and a sphere, Warme Stoffubertrag. 16 (3) (1982) 149–160.

[16] F.P Chiaramonti, A.J. Jitendra (Eds.), Workshop on Critical Issues in Microgravity Fluids, Transport, and Reaction Processes in Advanced Human Support Technology, Cleveland, OH, NASA/TM-2004-212940 (2005).

[17] E. Ungar, Single phase vs. two-phase active thermal control systems for space application: a trade study, AIAA 33rd Aerospace Science Meeting & Exhibit, Reno, NV, (AIAA 95-0634) (1995).

[18] Y.I. Grigoriev, E.I. Grigorov, V.M. Cykhotsky, Y.M. Prokhorov, G.A. Gorbenko, V.N. Blinkov, I.E. Teniakov, C.A. Maluhkin. Two-phase heat transport loop of central thermal control system of the international space station "Alpha" Russian segment, in: Proceedings of the 31st Heat Transfer Conference, Houston, TX, 1996. pp. 9–18. 1996.

[19] L.Chow, R. Parish, Condensation heat transfer in a microgravity environment, AIAA 24th Aerospace Science Meeting & Exhibit, Reno, NV, (AIAA-0068) (1986).

[20] S. Chandrasekhar, Hydrodynamic and Hydromagnetic Stability, Clarendon Press, Oxford, 1961.

[21] M.M. Weislogel, Fluid interface phenomena in a low-gravity environment: recent results from Drop Tower Experimentation, NASA Technical Report No. 19980221270.

[22] Z. Chen, Personal Communication (2004).

[23] S.V. Patankar, Numerical Heat Transfer And Fluid Flow, Hemisphere, Washington, DC, 1980.

[24] C. Yang, C. Chen, The boundary estimation in two-dimensional inverse heat conduction problems, J. Phys. D: Appl. Phys. 29 (1996) 333–339.

[25] A. Fröba, L. Penedo-Pellegrino, A. Leipertz, Viscosity and surface tension of saturated n-pentane, Int. J. Thermophys. 25 (5) (2004) 1323–1337.

[26] W. C Reynolds, Thermodynamic Properties in SI, Stanford University, 1979, pp 60–61, 145.

[27] S. Som, Stability and heat transfer characteristics of an unsteady condensing film, M.Sc Thesis, University of Washington, Seattle, WA, 2004.

[28] Y. Utaka, A. Saito, H. Yanagida, An experimental investigation of the reversibility and hysteresis of the condensation curves, Int. J. Heat Mass Transfer 33 (4) (1990) 649–659.